The International Journal of Advanced Manufacturing Technology
https://doi.org/10.1007/s00170-024-13649-x

ORIGINAL ARTICLE

The effect of surface roughness on the performance of 3D printed surface plasmon resonance sensors for refractive index measurements

Lorena Saitta[1] · Giovanni Celano[1] · Claudio Tosto[1] · Francesco Arcadio[2] · Luigi Zeni[2] · Claudia Sergi[3] · Nunzio Cennamo[2] · Gianluca Cicala[1]

Received: 4 November 2023 / Accepted: 15 April 2024
© The Author(s) 2024

Abstract
In this study, a polymer-based surface plasmon resonance (SPR) sensor for refractive index measurements was designed and manufactured via inkjet 3D printing; then, it was optically characterized. Next, it was investigated how the surface finish of the 3D printed optical waveguide affects the sensor performance, i.e., its sensitivity. More in detail, it was studied how the surface roughness changes with the placement of the 3D printed items on the building platform. To achieve this purpose, a Phase I distribution-free quality monitoring analysis of the selected manufacturing process was implemented for a small pilot production run. The aim was to check the stability of surface roughness versus the placement of the 3D printed parts on the building platform. The 3D printed sensor's surface roughness was assessed through a profilometry study. In particular, the surface roughness was determined for the core of the optical waveguide used to excite the SPR phenomena. Furthermore, the SPR sensors were optically characterized to find the existing relationship between their sensitivity and the considered quality of surface finish. In particular, by varying the surface roughness of the used waveguide, the light scattering in the waveguide changes, and the SPR sensitivity changes too, similarly to the light-diffusing fibers covered by gold nanofilms where the guided light is scattered through a plurality of voids distributed in the core. The procedure followed to investigate the sensor roughness, and establishing their performance enabled the optimal operative range for their application in practice to be identified. Finally, a better knowledge of the 3D printing manufacturing process has been achieved to improve quality of surface finish.

Keywords Additive manufacturing · Quality monitoring · Polymers · Sensor design · Plastic optical fibers · Plasmonic sensors · Roughness

1 Introduction

Over the last two decades, sensors and materials relying on the surface plasmon resonance (SPR) phenomenon have been used in several application fields, i.e., refractive index sensing [1, 2], toxin and small molecule sensing [3], food monitoring [4], clinical and molecular diagnostics [5–7], and environmental sensing [4, 8]. The SPR is a guided electromagnetic phenomenon that relies on a precise working principle (see Fig. 1): under a critical

✉ Lorena Saitta
lorena.saitta@phd.unict.it

Giovanni Celano
giovanni.celano@unict.it

Claudio Tosto
claudio.tosto@unict.it

Francesco Arcadio
francesco.arcadio@unicampania.it

Luigi Zeni
Luigi.ZENI@unicampania.it

Claudia Sergi
claudia.sergi@uniroma1.it

Nunzio Cennamo
nunzio.cennamo@unicampania.it

Gianluca Cicala
gianluca.cicala@unict.it

1 Department of Civil Engineering and Architecture, University of Catania, Viale Andrea Doria 6, 95125 Catania, Italy

2 Department of Engineering, University of Campania Luigi Vanvitelli, Via Roma 29, 81031 Aversa, Italy

3 Department of Chemical Engineering Materials Environment, Sapienza University of Rome, 00184 Rome, Italy

Published online: 03 May 2024

angle of incidence, when a light beam hits the interface between two transparent materials having at the interface a thin metallic layer, a component of the incident radiation interacts with the free electrons of the metal film, by causing them to resonate and thus generating a plasmonic wave upon the thin metal layer itself, which propagates in parallel with the metal–dielectric interface. So, since the energy possessed by the photons is fully transmitted to the electrons, a dark band in plasmonic reflectance spectra is found, which is a minimum named dip, dependent on the fixed incidence angle [9, 10].

When we have to deal with the SPR sensor fabrication, several parameters, such as the choice of the materials, the thickness of the deposited metal film, and the surface roughness, influence their final performance, like the sensitivity [11–14]. Among all these parameters, the surface roughness is the one that has been widely investigated in literature, because it is most affecting the sensor performance [15]. Previously, some inspections proved that a corrugated surface rather than a smooth one ensures a stronger photon-plasmon coupling, thus causing a raise in the concentration of the surface plasmon surface in proximity of the metal coating [16]. In line with this principle, Braundmeier and Arakawa [17] tried to increase the excited surface plasmon by exploiting rough metallic surfaces showing a roughness due to irregularities distributed in a random way. However, many other studies assess that a significant scattering of the light from the surface, due to a high surface roughness, negatively affects the sensor performance [18–21]. Treebupachatsakul et al. [22], who recently proposed a theoretical framework for analyzing and quantifying how the surface roughness affects the sensing performance of SPR measurements, proved that high surface roughness' height negatively affects the figure of merit for SPR sensors.

In agreement with what has been discussed so far, the studies reported in the state-of-the-art are mainly focused on the investigation of metal layer's roughness which, according to the main used functionalization technique, i.e., the sputter coating, has a root-mean-square (RMS) of 1.4nm up to 1.5nm [23]. This is justified by the fact that the widest manufactured and adopted SPR sensors exploit the Kretschmann (prism-coupled) configuration and consist of glass substrate, which is basically smooth, where a metal film is deposited [24]. Today, the latter configuration is the conventional one used for both commercial and bench-top SPR sensors, since it is a simple, sensitive, and robust approach. However, it also presents an important drawback: it is not suitable for miniaturization and integration. To overcome this issue, an innovative approach relying on planar optical waveguide structure is gaining ground. Saitta et al. [25, 26] have already developed micro-structured SPR sensors exploiting a planar approach, based on inkjet 3D printing and using photocurable resins with tailored refractive index, which allowed for temperature and refractive index measurements. Since the latter proposed approach relies on a SPR sensors composed of a photocured resin substrate rather than a smooth glass one, it is of crucial importance to analyze how the surface roughness of the 3D printed part (prominent with respect to the metallic layer one) affects the developed planar optical SPR sensor. Hence, starting from the state-of-the-art status argued so far, at first, this experimental work investigated the surface roughness of the 3D printed SPR sensor through a profilometry test performed using a profilometer. Secondly, to test the stability of the surface roughness as a quality performance measure for a small batch of trial production manufactured through the selected inkjet 3D printing technique, a Phase I distribution-free quality monitoring investigation based on a recursive sequential and permutation (RS/P) procedure was exploited. Indeed, when

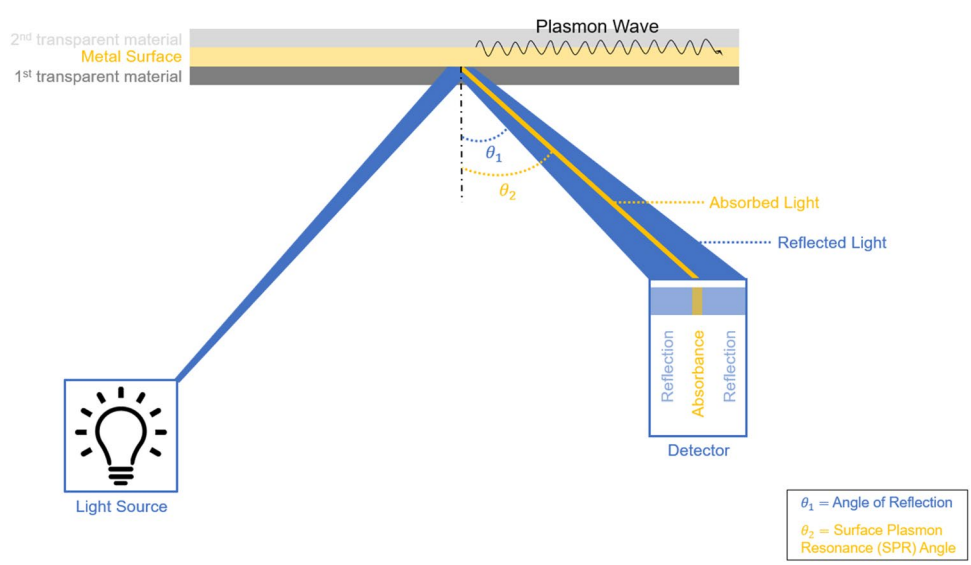

Fig. 1 Surface plasmon resonance (SPR) working principle schematization

we have to deal with the 3D printing techniques, the quality of the final product, i.e., the surface roughness, depends on many process parameters, like the orientation of the part on the building platform, the gantry velocity for positioning the printhead, and the printhead movements carried out to manufacture the desired part [27–30]. Generally, analyzing the surface quality of the 3D printed item in relation to the latter parameters is a practice performed for the FFF (Fused Filament Fabrication) and FDM (Fused Deposition Modeling) techniques. Conversely, only a few studies have been run for the inkjet 3D printing technique. All of them have been carried out with the aim to investigate how several parameters are influential on 3D printed items' surface roughness. These are (i) layer thickness [31, 32]; (ii) build orientation [31, 33–37]; (iii) finish type or build style [31–33, 35, 37]; (iv) scale of the model [32]; (v) post-processing procedure [35]. Furthermore, none of these studies related the surface roughness measurements conducted on the 3D printed parts to their functionality. In fact, they are related to an evaluation and/or optimization of the surface finish quality for rapid prototyping. Alternatively, mechanical properties have been considered, but no mention has been made regarding the optical properties correlated to the SPR phenomenon investigated in our study.

According to what has been argued so far, the novelty of this research study consists in investigating how the surface roughness of the 3D printed sensors, which is related to their placement on the building platform of the 3D printing machine, affects theirs optical performance. More in detail, this paper aims to expand upon the outcomes of our prior work [26], in which we have proposed a new design and manufacturing strategy for a low-cost SPR sensor suitable for refractive index measurements exploiting a planar configuration. Here, we have also assessed its feasibility by using the Inkjet 3D printing technology, by achieving good performances, in terms of figure of merit (FOM), i.e., very similar to other SPR sensors made using plastic optical fibers (POFs). While, innovatively building upon our previous mentioned research, in this work we have manufactured many items through the already selected manufacturing technique. We intentionally considered different placements on the building platform with the aim to investigate the stability of the surface roughness for all sensors. This stability has been assessed by running a Phase I distribution-free quality monitoring investigation named recursive sequential and permutation (RS/P) procedure. Additionally, we have investigated how this parameter affects the fabricated SPR sensor's performance, by leaving unchanged the previously proposed design and manufacturing approach. Thus, referring to the research [26] as the starting point, a step forward has been taken by manufacturing a small batch of trial production of planar SPR sensors on the same job by allocating them across different positions of the building platform. The purpose was to inspect how the surface roughness of the fabricated objects is affected by their position and, consecutively, by the *XY*-axis movements performed by the printhead machine. For our application, this kind of investigation is of paramount importance, since the inkjet 3D printing technique relies on the liquid droplet deposition on the building platform. This deposition is related to a complex physical process, because the injected droplet falls on the substrate; next, it spreads and it is subjected to retraction and oscillation phenomena [30]. Thus, it is worth investigating how the *XY*-axis movements of the used 3D printing machine's printhead affect the droplet deposition process on the building platform with the intention to evaluate a possible uneven droplet distribution which, as result, causes the manufacturing of a defective device. For this reason, the fabricated SPR sensors were optically characterized to find the existing relationship between their sensitivity and the considered quality of surface finish.

The paper is organized as follows. In Sect. 2, we present the materials used to manufacture the 3D printed SPR sensor (Sub-Sect. 2.1) and the methods followed to design and manufacture the sensor (Sub-Sect. 2.2), to analyze the surface roughness of the 3D printed part through profilometry test (Sub-Sect. 2.3), and to perform quality monitoring of the 3D printed surface's roughness using the RS/P procedure (Sub-Sect. 2.4) and the experimental setup used to test the developed SPR sensors together with the experimental campaign run to determine their performance (Sub-Sect. 2.5). The obtained results are reported in Sect. 3. In detail, the results relative to the Phase I RS/P procedure investigating quality of surface roughness are commented in Sub-Sect. 3.1, while the results regarding the optical characterization of the SPR sensors and their performance determination are discussed in Sub-Sect. 3.2. Finally, conclusions and future research directions are reported in Sect. 4.

2 Materials and methods

2.1 Materials

The SPR sensors were fabricated by using three different resins: VeroClear RGD810 (OVERMACH S.p.A., Parma, Italy), FullCure705 (OVERMACH S.p.A., Parma, Italy), and NOA88 (Edmund Optics, Nether Poppleton York, UK).

VeroClear RGD810 is an acrylic liquid photopolymer with a refractive index of 1.531 at 650 nm. This resin has a heat distortion temperature (HDT) of 45 – 50 °C, so it is stiff at room temperature. It also has a tensile modulus of 2.5 GPa. The Material Safety Data Sheet (SDS) shows that the resin is a complex mixture of acrylate monomers and photoactivators. The formulation was developed by Stratasys specifically for PolyJet 3D printing. The cladding of the SPR sensor was 3D printed using VeroClear RGD810 resin on a *Stratasys Objet260 Connex1* 3D printer (Stratasys, Los Angeles, CA, USA).

FullCure705 is the resin that was used as removable support. This resin is a mixture of acrylic liquid photopolymer; polyethylene glycol; propane-1,2-diol; and glycerol used in the printing process with the function of detachable support. Indeed, FullCure705 is simply removed by water jet after the printing process.

NOA88 is an optical clear adhesive required to fill the channels of the printed device. In fact, NOA88 serves to manufacture the optical waveguide, i.e., the core of the designed SPR sensor. NOA88 is a low-viscosity (250 cps) UV curing adhesive with a refractive index of 1.56 at 589 nm. The refractive index of NOA88 is precisely the key parameter that allows to obtain a POF (polymer optical fibers), as it is superior to the refractive index of the VeroClear RGD810 resin. This resin has an absorption between 315 and 395 nm, so it was UV cured using a universal lamp with UVA emission (365 nm). The Material Safety Data Sheet (SDS) for NOA88 shows a composition based on a blend of a proprietary mercapto-esters blended with triallyl isocyanurate.

2.2 SPR sensor design and manufacturing process

The design of the SPR sensor for refractive index measurements was developed starting from a previous version already proposed by the authors in another paper [26]. Hence, it consists of four assembled parts, i.e., (i) the substrate (bottom part) which contains the waveguide core: the trench filled by optical adhesive [26] (see Fig. 2a); (ii) the supports to guarantee the alignment between the input and output plastic optical fibers (POFs) with the sensor's waveguide core (see Fig. 2b); (iii) a cover used to preserve the sensing region during the storage time (see Fig. 2c); and (iv) a customized mask properly designed to cover the waveguide core with metal nanofilms through a sputtering process (see Fig. 2d). Figure 2e shows the assembled sensor chip with its components. The process flow to manufacture the sensor and its geometry are already described in a previous paper by the authors [26].

Each part reported in Fig. 2 was fabricated using the PolyJet 3D printer Stratasys Objet260 Connex 1. In order to realize the waveguide core of the SPR sensor chip, a NOA88 photocurable adhesive was micro-injected within the channel shown in Fig. 2a and photocured using an universal lamp bulb with UVA emission at 365nm, as formerly discussed in [26].

Next, the waveguide core was properly covered by a gold nanofilm via a sputter coater machine (model CCU-010, manufactured by Safematic, Zizers, Switzerland). During the sputtering process, the mask reported in Fig. 2d was used. The deposited gold nanofilm on the core presents a thickness of 60 nm [26].

In this study, a step forward with respect to the aforementioned previous work [26] has been taken by 3D printing $m = 5$ different items on the same job, i.e., by allocating them across different positions of the building platform (see Fig. 3), with the aim to investigate how the surface roughness of the fabricated objects is affected by their position and, consecutively, by the *XY*-axis movements performed by the printhead machine, being the *X*-axis movements performed from left to right and vice versa, while the *Y*-axis ones from front to back and vice versa. Investigating the latter aspect is crucial, since the inkjet 3D printing technique relies on the liquid droplet deposition on the building platform, with a precise flow which consists of a complex physical process interesting different kinds of energies (i.e., gravitational potential, kinetic, viscous dissipation, and surface free energy) [30]. Indeed, the injected droplet falls by impacting toward the substrate, next spreads, and it is subjected to retraction and oscillation phenomena. In the-state-of-the-art, many studies have already investigated the latter behaviors for flat solid surface [38–41] because, in the field of functional additive manufacturing, the final functional

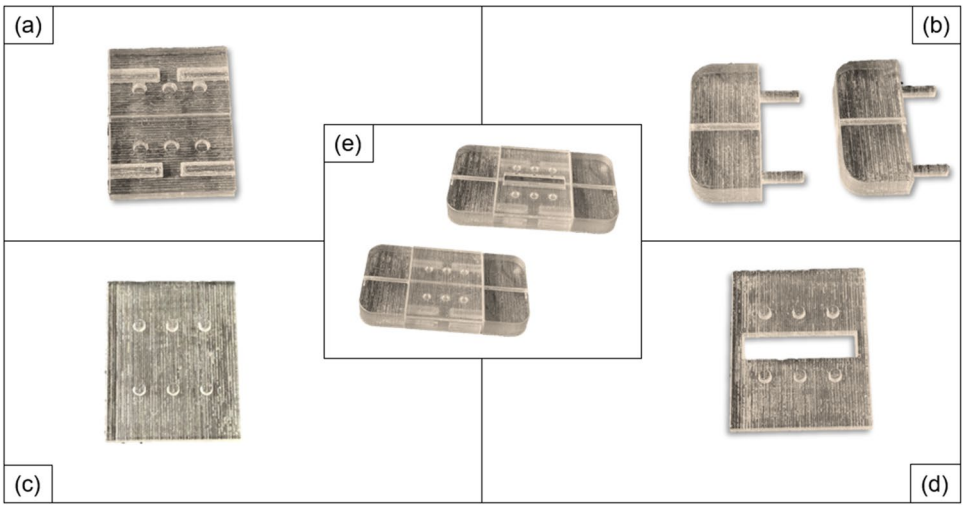

Fig. 2 3D-printed parts in VeroClear RGD810: substrate (**a**), plastic optical fiber (POF) supports (**b**), cover for storage (**c**), and mask for sputtering (**d**). Two different configurations, using either the mask or the cover, of the assembled SPR sensor by properly assembling all the fabricated parts (**e**)

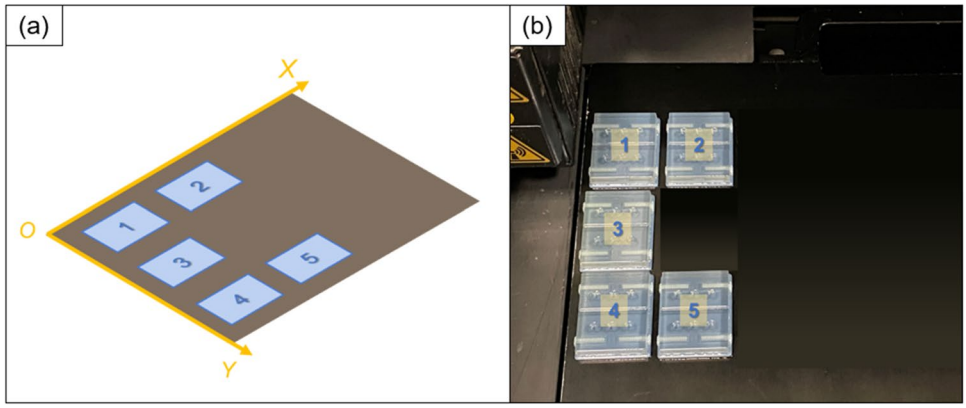

Fig. 3 Upper view schematization (**a**) and real picture (**b**) of the manufactured parts placement on the building platform

device performance is strictly dependent on the final surface morphology. So, we followed this approach to investigate how the printhead's *XY*-axis movements affected the droplet deposition process and to evaluate a possible uneven droplet distribution, hence causing the manufacturing of a defective device. To achieve this aim, the items were placed on the building platform in such a way to record the printhead *XY*-axis movements in an easy way.

About the relationship between surface roughness and the stability of 3D printed SPR sensors for precise refractive index measurements, the SPR chip stability does not change during the RI (refractive index) measurements because the surface having the roughness of interest is coated by the sensing multilayer (optical adhesive and metal nanofilm).

2.3 Surface roughness measurements

The surface roughness for the floor of the waveguide's channel was assessed through profilometry by using a profilometer Talyscan 150 by Taylor Hobson equipped with a direct contact probe Form Talysurf, which is an inductive meter (Fig. 4a). A scan speed of 3000 μm/s and 5 μm spacing along both *X* and *Y* directions were selected to map the surfaces. The resulting profiles were analyzed with the Talymap 3D software to obtain the 3D reconstruction of the investigated surface and to estimate the roughness. In detail, due to the difficult accessibility to the sensor's channel, an indirect measure of its floor's roughness was carried out on the parallel upper surface of the 3D printed substrate, as indicated in Fig. 4b. It is reasonable to run such an indirect measurement of the roughness, since both the upper and floor surfaces of the waveguide's channel are the latest layers jetted and photocured by the printhead. The coordinate observations of roughness y_{jk} of $m = 5$ SPR sensors have been collected by splitting their upper surface into $a = 8$ different areas A_{jk} with $j = 1, \dots, a$ and $k = 1, \dots, m$, as illustrated in Fig. 4c. Each investigated area has a size of 5.5×3 mm^2. For each area, $i = 1$ observation has been collected.

Then, the following measures of surface roughness have been calculated for each investigated area A_{jk}:

(i) Roughness average $R_{a_{jk}}$ (see Fig. 5a)—it is the arithmetic average of the absolute values of the roughness profile ordinates. It provides a good general description of the height variations in the surface.

(ii) Root mean square roughness $R_{q_{jk}}$ (see Fig. 5b)—it is the root mean square average of the roughness profile ordinates.

(iii) Roughness $R_{z_{jk}}$ (see Fig. 5c)—it is the distance between two lines parallel to the average line passing between the five highest peaks ($Z_{p1}, Z_{p2}, Z_{p3}, Z_{p4}, Z_{p5}$) and the five lowest valleys ($Z_{v1}, Z_{v2}, Z_{v3}, Z_{v4}, Z_{v5}$), within the limits of the base length. Next, to calculate the R_z parameter, the average absolute height (Z_p) of the five highest peaks and the average absolute height (Z_v) of the five deepest valleys, both measured from the mean line, are considered. These two values are then summed.

(iv) Roughness $R_{t_{jk}}$ (see Fig. 5d)—it is the sum of the maximum peak height (Z_p) and the maximum measurement of the deepest valley (Z_v) in the evaluation length (5.5 mm).

More insights related to the four different calculated and investigated parameters of surface roughness are reported in the sub-section S1.1. Supplementary materials: Surface Roughness Measurements.

2.4 Quality control of the 3D printed surface's roughness

The quality of the manufactured SPR sensors is measured by their surface measures of roughness, as it significantly influences their performance. To test the stability of surface roughness for all sensors, a Phase I distribution-free quality monitoring investigation has been carried out by running a

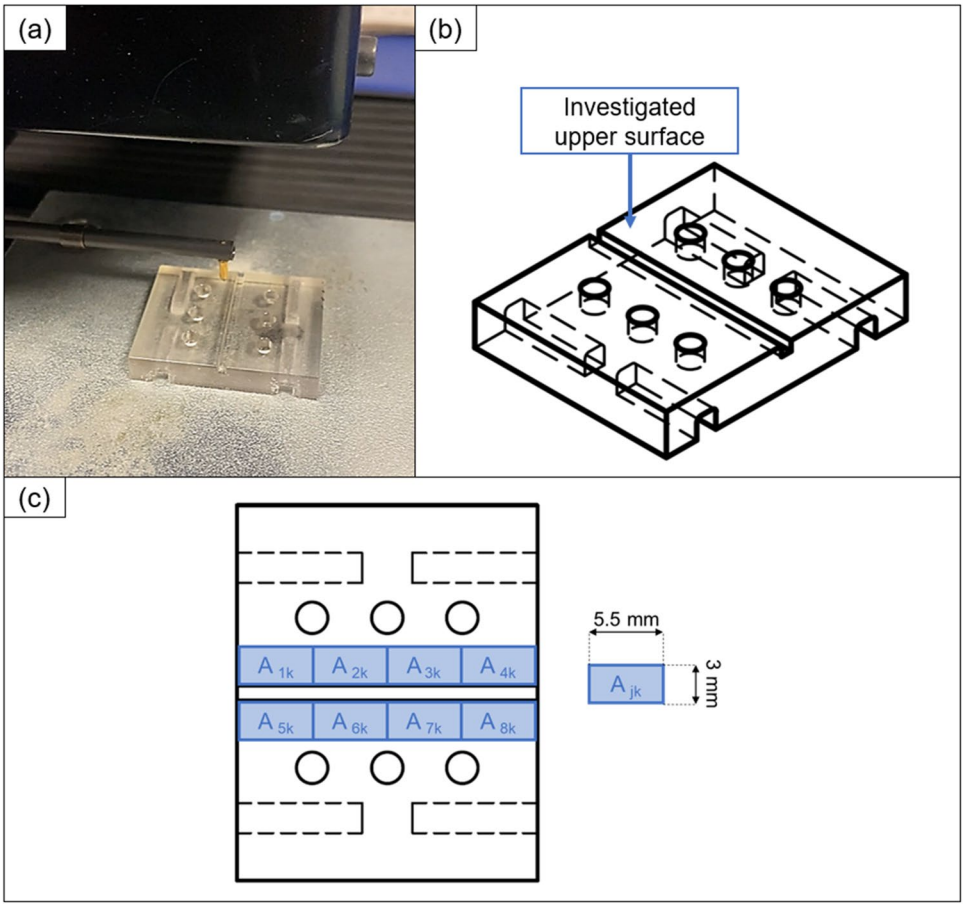

Fig. 4 Surface roughness measurements run using a profilometer Talyscan 150 by Taylor Hobson (**a**) on the upper surface of the 3D-printed surface (**b**) and by analyzing $a = 8$ different areas of size 5.5×3 mm^2 (**c**)

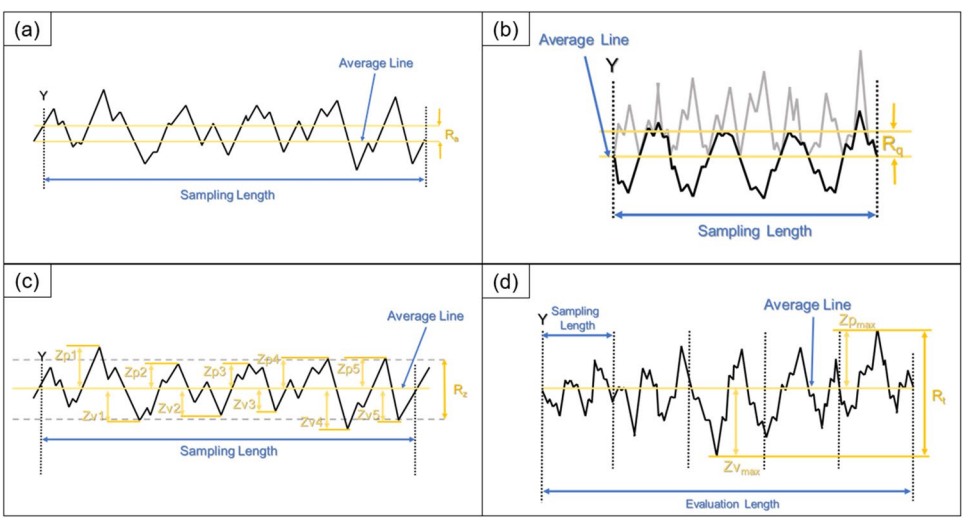

Fig. 5 Schematization of the R_a (**a**), R_q (**b**), R_z (**c**), and R_t (**d**) calculation

recursive sequential and permutation (RS/P) procedure proposed by Capizzi and Masarotto [42]. The advantage related to implementing this procedure is that it does not require any preliminary knowledge about the distribution of roughness observations. The RS/P procedure allows process changepoints (CPs) either in location and/or scale of the observed parameter to be detected. A changepoint in process location (scale) is an undesired shift occurring to the median (dispersion) the measures of roughness observations. All the available SPR sensors have been controlled for quality. Being a Phase I retrospective study, all the surface roughness measures collected for each manufactured SPR sensor have been investigated by accounting for each sensor location on the 3D printing build platform and the time order of production,

which is defined by the movement of the printing head. In the absence of process changepoints, the RS/P procedure confirms the 3D printing process stability with respect to the sensor surface quality. A flow chart of the quality control procedure is shown in Fig. 6.

Quality control of SPR sensors has been carried out as follows:

Step 1. *Definition of the items order of production and their placement on the building platform*. To check the stability of the observed roughness for each SPR sensor's surface, the order of production of the 3D printed parts and their placement on the building platform are recorded. The *XY* movements of the printhead above the building platform to manufacture each 3D printed part are schematized in Fig. 7. An identification number is assigned to each part placed on the building platform, as shown in Fig. 3.

Step 2. *Presence of outliers*. The presence of one or more isolated outlier measures of roughness should be investigated and any identified outlier point should be removed to obtain a clean dataset of the collected observations: thus, the Grubb statistical test can be implemented for the purpose. The results are discussed in the sub-section S1.2. Supplementary materials: Quality Control.

Step 3. *Recursive segmentation and permutation (RS/P) analysis.* For each sensor, the measures of roughness are calculated within each area A_{jk} with $j = 1, \ldots, a$ and $k = 1, \ldots, m$. Then, the RS/P method is implemented on each measure of roughness by means of the *dfphaseI*

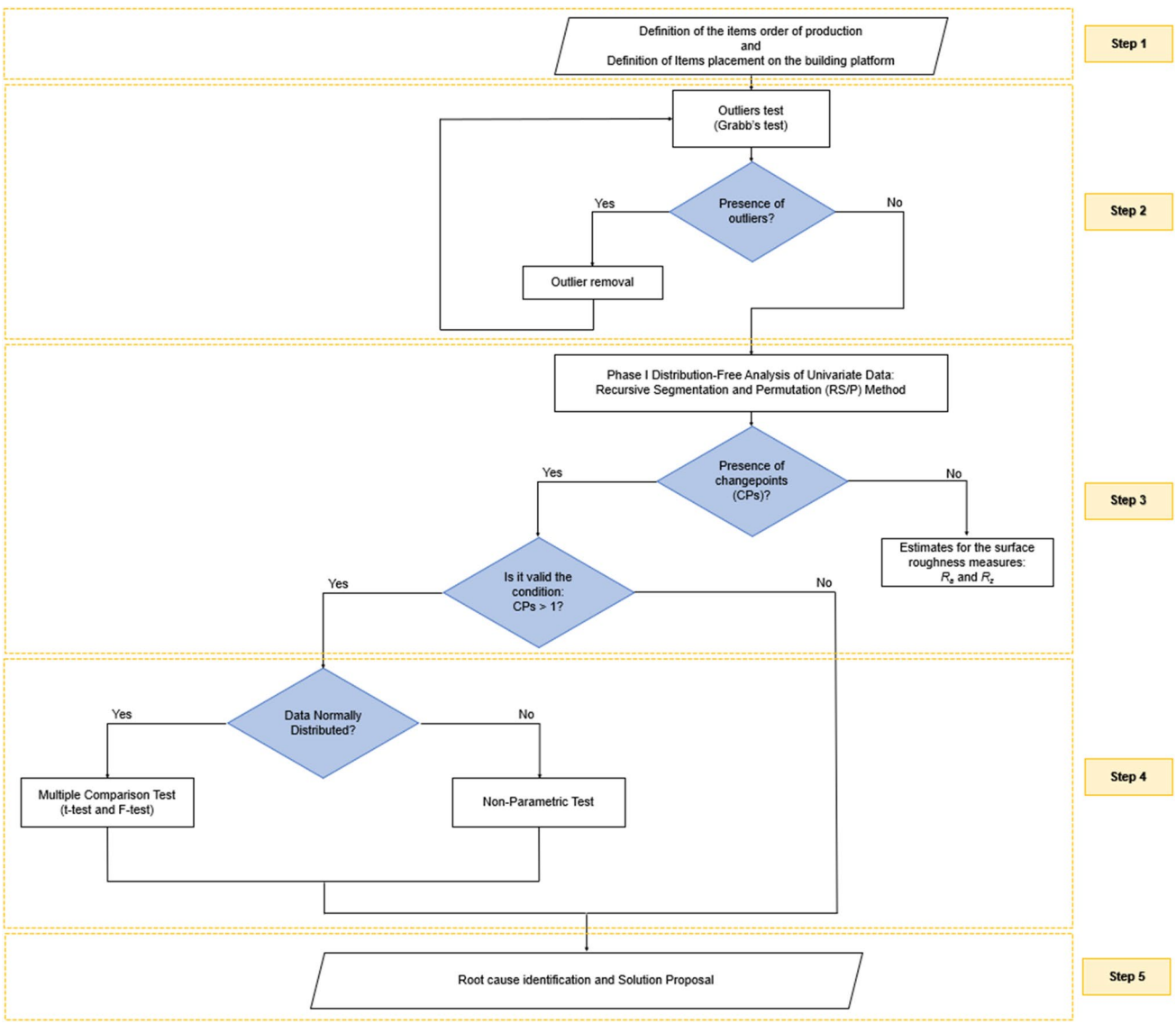

Fig. 6 Flow chart of the implemented Phase I RS/P quality monitoring procedure

package made available on R (R Development Core Team (2012)) from Capizzi and Masarotto [42]. If the RS/P procedure does not reveal any changepoint in the process, then it is possible to get reliable estimates of each measure of surface roughness of the SPR sensors. Otherwise, further investigation is needed to understand why the process performance deteriorated. The presence of one or more process changepoints should be investigated to look for the assignable causes leading to a shift in the location and/or scale. First of all, it is necessary to identify the observation where the process changepoint has been triggered by the RS/P procedure. The shift can occur either within a sensor, i.e., among adjacent areas on the same part, or between sensors. In the first case, the root cause could be restricted locally to the area interested by the shift. In the second case, clusters of parts can be identified according to their position within the 3D printing machine working volume, thus revealing a more complex problem related to the 3D printing process.

Step 4. *Multiple comparison test.* If the number of process changepoints between parts is CPs > 1, then a multiple comparison test (if the observations are normally distributed), or a non-parametric test (if the observations are not normally distributed), is run to identify clusters of parts. This step of the proposed method is pivotal to identify the effect of each item's location above the build plate on the surface roughness quality.

Step 5. *Root cause identification and solution proposal.* Based on quality monitoring performed above, a root cause identification is required to solve issues related to the location of the 3D printed SPR sensors during the 3D printing process.

The statistical analyses proposed in the procedure described so far were performed by using both the R and Minitab® software.

2.5 Polymer-based SPR sensor: experimental setup and experimental characterization

The conceived SPR sensor was tested using an experimental setup based on a spectral mode configuration: (i) a halogen lamp as white light source (model HL-2000-LL, manufactured

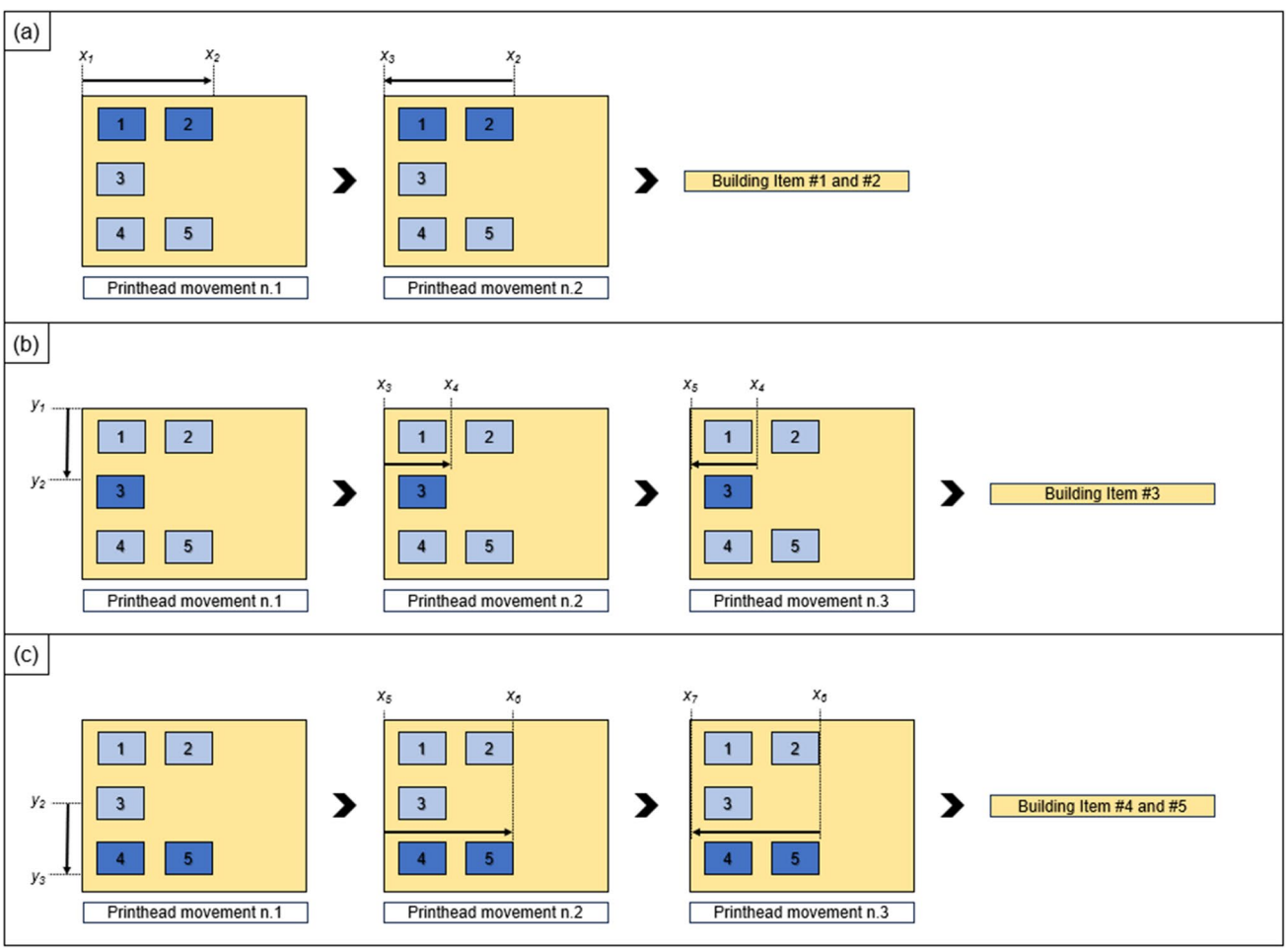

Fig. 7 Sequence of the printhead *XY* movements to manufacture items #1 and #2 (**a**), #3 (**b**), #4 and #5 (**c**)

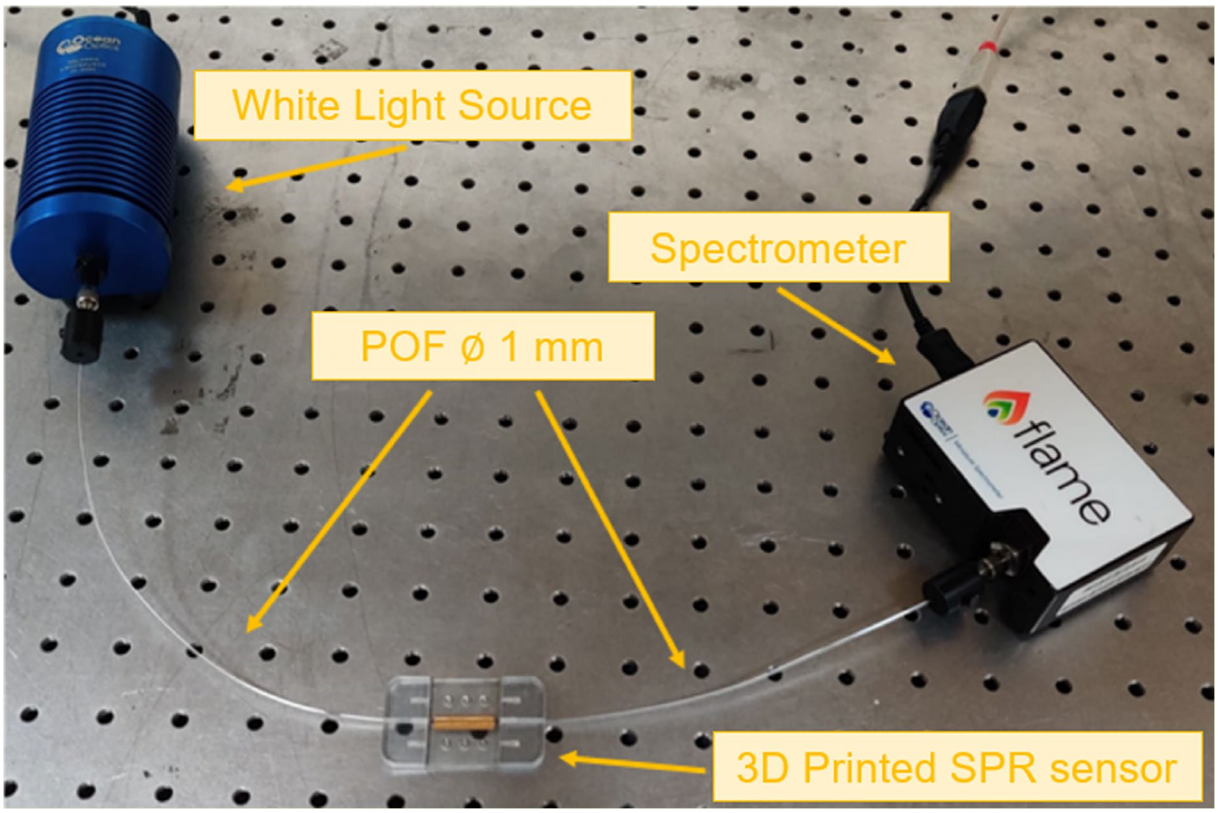

Fig. 8 Picture of the experimental setup for 3D printed surface plasmon resonance (SPR) sensors

by Ocean Optics, Dunedin, FL, USA) having an emission range between 360 and 1700 nm; (ii) two patches of plastic optical fibers (POFs) of 1 mm of total diameter size (with a core of PMMA), which were used to illuminate the waveguide core of the SPR sensor chip and to collect the transmitted light at the output; and (iii) a spectrometer connected to a laptop (model FLAME-SVIS-NIR-ES, manufactured by Ocean Optics, Dunedin, FL, USA) with a detection range from 350 up to 1023 nm. The entire experimental setup is shown in Fig. 8.

To evaluate if there is any interaction between the location on the 3D printer's building platform of the manufactured sensors and their surface's roughness and if there is any interaction between the latter parameter (surface's roughness) and the SPR sensor performance, expressed as bulk sensitivity, several liquids with different refractive indices are used to obtain the sensor sensitivity for each 3D-printed sensor with different surface roughness (a total of 5, see Sub-Sect. 2.4.).

In detail, to carry out the bulk solutions useful to test the SPR sensors, several mixtures of water-glycerine characterized by different refractive index values (n), ranging between 1.332 and 1.383, were used as surrounding medium for the gold nanofilm deposited upon the polymer waveguide. For each used mixture, the exact refractive index value was previously determined with an Abbe refractometer (Model RMI, Exacta + Optech GmbH, Munich, Germany).

In the end, in order to compare the performances of the sensors with different surface roughness, the bulk sensitivity was determined (S_n). The latter parameter was evaluated by considering the shift in resonance wavelength per unit change in the refractive index of the bulk ($S_n = \Delta\lambda/\Delta n$).

3 Results and discussion

3.1 Quality control

In this section, the obtained results from the Phase I RS/P retrospective study are commented. More details for each step of the carried out analysis are provided in the sub-section S1.2. Supplementary materials: Quality Control. At first, since the measures of roughness are correlated in pairs per investigated item, i.e., R_a is correlated with R_q and R_z is correlated with R_t, (see the matrix plot on Fig. 9), for the sake of brevity, the Phase I analysis has been carried out only on R_a and R_z.

The Phase I control charts obtained by implementing the RS/P procedure are shown in Figs. 10 and 11 for the R_a and R_z measurements, respectively. According to the RS/P analysis outcome, two changepoints, i.e., a shift in the location (p-value = 0.004 < 0.05, at point #14) and in the scale (p-value = 0.018 < 0.05, at point #15),

have been identified for the R_a parameter (see Fig. 10). Similarly, even for the parameter R_z, two changepoints in location (p-value = 0 < 0.05, at point #16) and scale (p-value = 0 < 0.05, at point #16) have been identified 9 see Fig. 10).

The obtained results reveal a between-part instability affecting the manufacturing process, since two changepoints occur between parts #2 and #3 and between parts #4 and #5 for both R_a and R_z (see Figs. 10 and 11). Therefore, the 3D printed items can be clustered together in terms of surface roughness: *cluster 1*, including sensors #1 and #2; *cluster 2*, including sensors #3 and #4; and finally, *cluster 3*, consisting of item #5. For each cluster, the estimated mean (μ) and standard deviation (σ) values for R_a and R_z are reported in Table 1.

The obtained results show that the item position on the building platform affects the measures of roughness R_a and R_z. Looking at the estimated means for R_a and R_z (dotted lines in Figs. 10 and 11), they look very similar between the *cluster 1* of items #1 and #2 and *cluster 3*, including item #5. Therefore, two-sample hypothesis tests have been considered to decide if *clusters 1* and *3* can be merged. Normality of the R_a and R_z observations from the two clusters has been checked by means of an Anderson–Darling test (p-value > 0.05), as shown in Figure S4 and Figure S5 in the Supplementary materials. Then, a F-test has been carried out to assume equal variances between the two considered clusters (p-value > 0.05). Finally, a t-test for the difference in the means has been performed. The obtained results for each test are shown in Tables 2 and 3 for the measures of roughness R_a and R_z, respectively.

According to the results shown in Tables 2 and 3, both the cluster mean and variance of the measure of roughness R_a for items #1 and #2 (*cluster 1*) are not statistically different from the item #5 (*cluster 3*), (p-values > 0.05). Thus items #1, #2, and #5 can be considered belonging to the same cluster with an estimated R_a value of 0.93 ± 0.02 μm. Conversely, items #3 and #4 must be considered part of a different cluster, with an estimated specification R_a equal to about 1.21 ± 0.05 μm. A similar outcome was found for the measure of roughness R_z. Indeed, the tests proved that items #1, #2, and #5 are part of the same cluster with a R_z value of 9.05 ± 0.33 μm. Conversely, items #3 and #4 belong to a different cluster having an estimated R_z value equal to 19.77 ± 1.34 μm.

An explanation to this issue can be found by making a point about the item's placement on the building tray of the 3D printing machine, which is linked to the *XY*-axis movements performed by the printhead to fabricate each item. Indeed, to manufacture the first cluster of items, i.e., #1, #2, and #5, just a one-direction motion (along *X*-axis) is required (see Fig. 7a and c). Conversely, to build the second cluster of items, that is, #3 and #4, a combination of motions along two different directions (i.e., along *X*-axis and along *Y*-axis) is performed (see Fig. 7b and c, respectively). This means that the rate of positioning of the printhead is not fully commensurate to the rate of material jetting from the inkjet nozzle when fast movements along the two perpendicular directions (*X*-axis and *Y*-axis) are necessary to manufacture a 3D printed part. The latter situation is attributed to the fast printhead movements which cause its motors to skip steps, so bringing to a loss of accuracy. A similar issue was already pointed out for the FDM 3D printing technique. Indeed, Go et al. [27] have highlighted that when the actuators are commanded beyond their maximum speed and/or acceleration, stepper motors result to be driven without feedback,

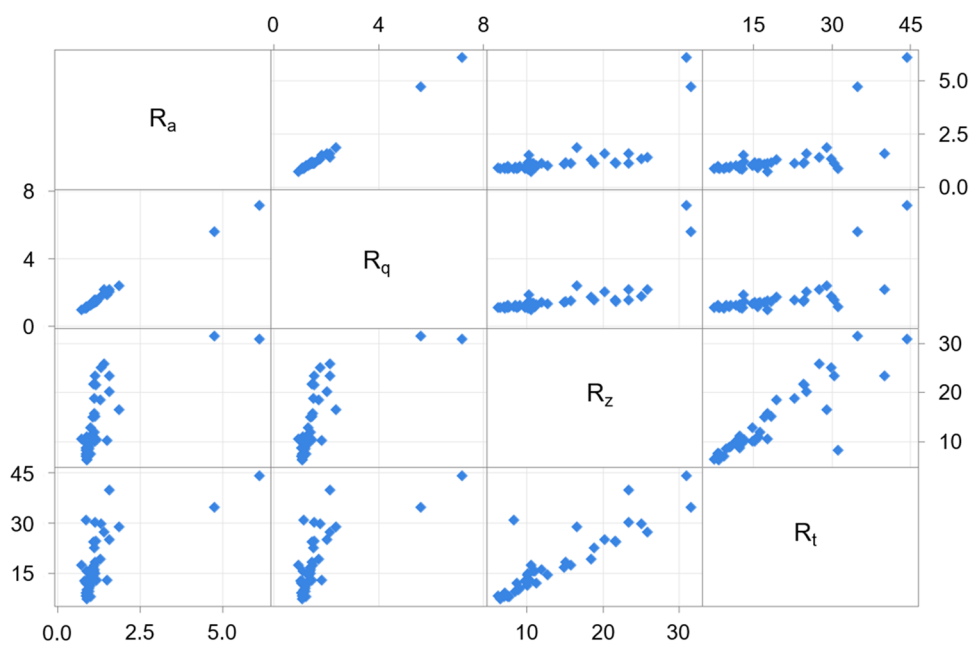

Fig. 9 Matrix plot of the collected measures for R_a, R_q, R_z, and R_t

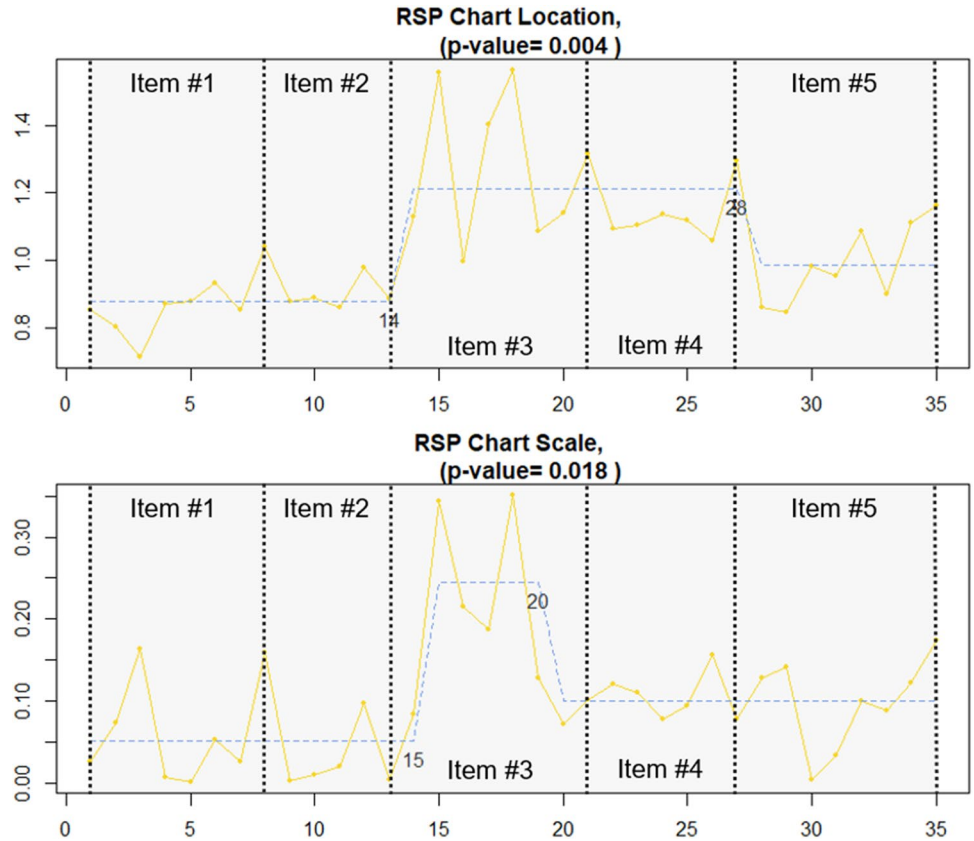

Fig. 10 Phase I RS/P procedure for the R_a measurements: location chart (upper panel) and scale chart (lower panel)

so receiving movement commands beyond their operating performance range and causing the motors to skip steps resulting in loss of accuracy in turn. The latter explanation provided for the FDM technique fits well even with the findings made in our study. Indeed, the mechatronic movement system, named gantry, which has the task to convert rotational motion into linear one to move the printhead along the toolpath imposed by the G-code to create motion *X*-axis and *Y*-axis movement, is the same both in FDM and inkjet 3D printing techniques. Basically, it relies on the use of servo motor, belts and pulleys. In detail, two belts are used, one for each axis (*X* and *Y*), as shown in Fig. 12 for the Stratasys Objet260 Connex1 3D printer used in our study.

The explanation proposed here is justified by the 3D surface reconstruction for both the two clusters, which are shown in Fig. 13, respectively. It is evident from panels (**a**), (**b**), and (**e**) that the distribution of both the peaks and valleys is more uniform when only a one-direction movement along the *X*-axis is required to realize the 3D printed part. Indeed, while for the cluster of items #1, #2, and #5 the reconstructed morphology follows and confirms the deposition of droplets by the printhead injection (see Fig. 13a, b, and e), a surface characterized by uneven droplet distribution with thin irregular spikes is revealed for items #3 and #4 (Fig. 13c and d), which in the end causes a higher surface roughness.

3.2 Optical characterization of SPR sensors

The obtained results from the experimental characterization of the SPR sensors belonging to each identified cluster of production are reported in this section.

Figure 14a shows the experimentally determined SPR spectra for the 3D printed item #1. The SPR spectra are obtained by normalizing the transmitted spectra acquired with different solutions to the reference spectrum (acquired with air as the surrounding external medium). It must be highlighted that the higher the refractive index of the water-glycerine solution, the higher the SPR wavelength. By using the spectra reported in Fig. 14a and b reports for the 3D printed item #1 the wavelength resonance variations ($\Delta\lambda$), calculated with respect to water ($n = 1.332$), versus the refractive index along with the linear fitting of the experimental data.

The functional relationship existing between $\Delta\lambda$ and the refractive index (n), which was experimentally determined for the item #1, is reported below:

$$\Delta\lambda^{(1)} = \beta_0^{(1)} + \beta_1^{(1)} n^{(1)} \quad (1)$$

being each term expressed in Table 4 both in terms of estimated value and standard error.

In a similar way, for the 3D printed item #4, Fig. 15a shows the experimentally determined SPR spectra obtained at

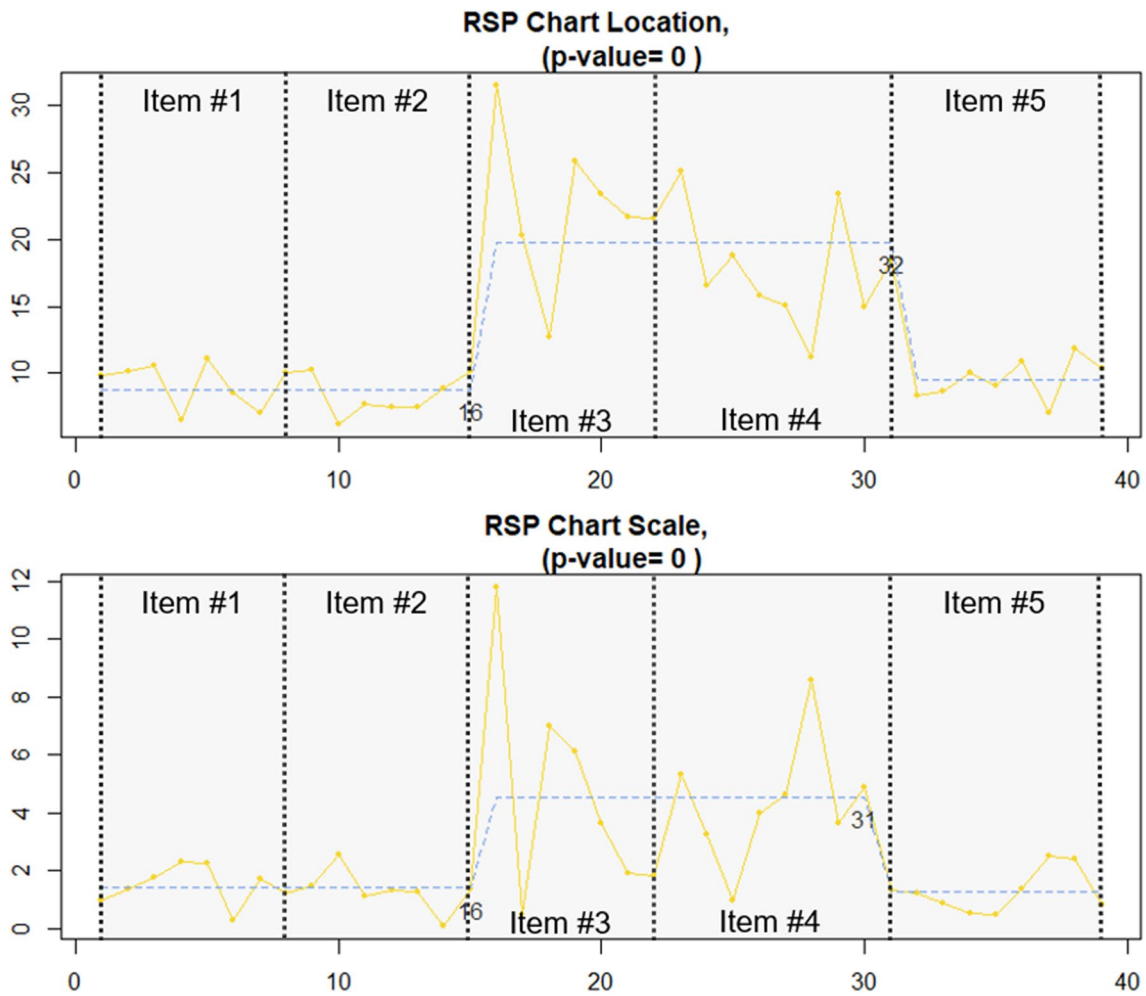

Fig. 11 Phase I RS/P procedure for the R_z measurements: location chart (upper panel) and scale chart (lower panel)

Table 1 Estimated mean value μ and standard deviation σ for R_a and R_z determined for each cluster

	R_a		R_z	
#Cluster	μ (μm)	σ (μm)	μ (μm)	σ (μm)
1 (items #1 and #2)	0.8794	0.0526	8.7895	1.4066
2 (items #3 and #4)	1.2139	0.2449	19.7725	4.5245
3 (item #5)	0.9873	0.1007	9.5269	1.2775

Table 2 *F*-test and the *t*-test between clusters 1 and 3 for the R_a measure of roughness

Method	Statistic	df_1	df_2	*p*-value
F-test	0.70	13	7	0.547
Pooled *t*-test	− 1.89	14	8	0.074

Table 3 *F*-test and the *t*-test between clusters 1 and 3 for the R_z measure of roughness

Method	Statistic	df_1	df_2	*p*-value
F-test	1.04	14	7	0.992
Pooled *t*-test	− 1.06	15	8	0.303

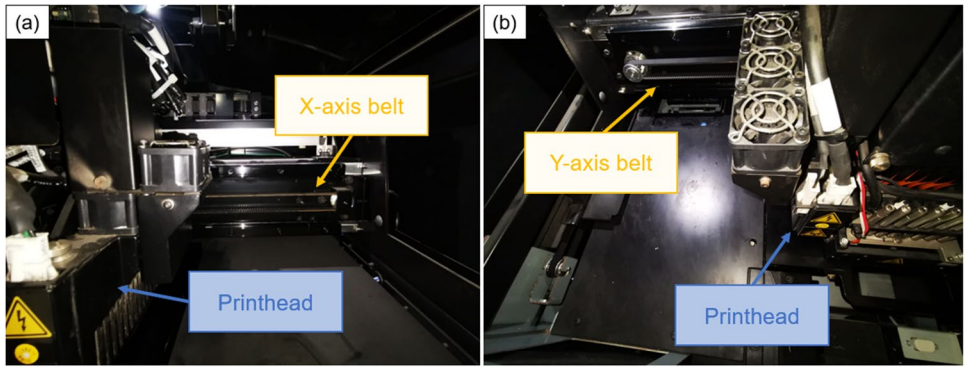

Fig. 12 *X*-axis (**a**) and *Y*-axis (**b**) belts of the Stratasys Objet260 Connerx1 3D printer's gantry system

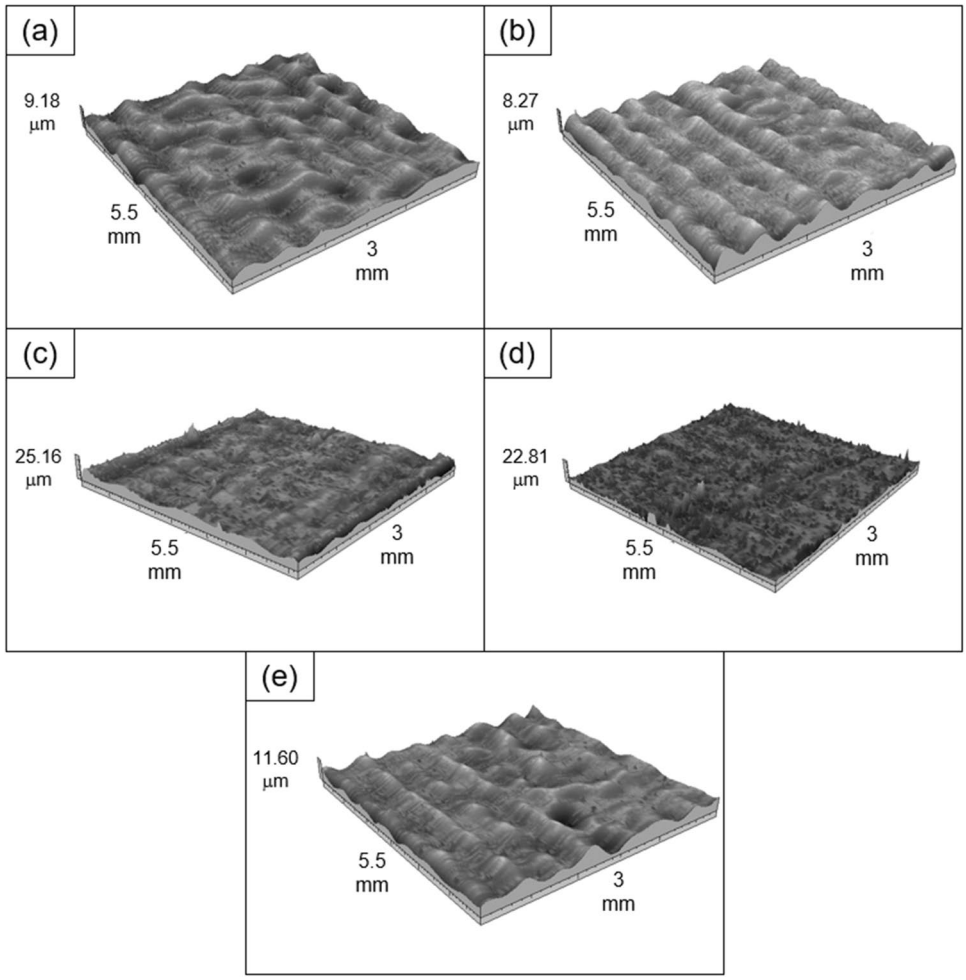

Fig. 13 3D surface reconstruction for the investigated areas: A_{17}, item #1 (**a**); A_{22} item #2 (**b**); A_{22} item #3 (**c**); A_{22} item #4 (**d**); A_{53} item #5 (**e**)

different refractive index values, whereas the resonance wavelength variation ($\Delta\lambda$) versus the refractive index is reported in Fig. 15b along with the linear fitting of the experimental data.

The functional relationship existing between $\Delta\lambda$ and the refractive index (n), which was experimentally determined for the item #4, is reported below:

$$\Delta\lambda^{(4)} = \beta_0^{(4)} + \beta_1^{(4)} n^{(4)} \tag{2}$$

being each term expressed in Table 5 both in terms of estimated value and standard error.

The sensors' sensitivities (S_n) can be estimated by evaluating the first derivative of the obtained linear fittings for both tested items #1 and #4; thus, they correspond to the slopes of the fitted lines.

According to the obtained results, it must be highlighted that the SPR sensor characterized by a higher value of roughness

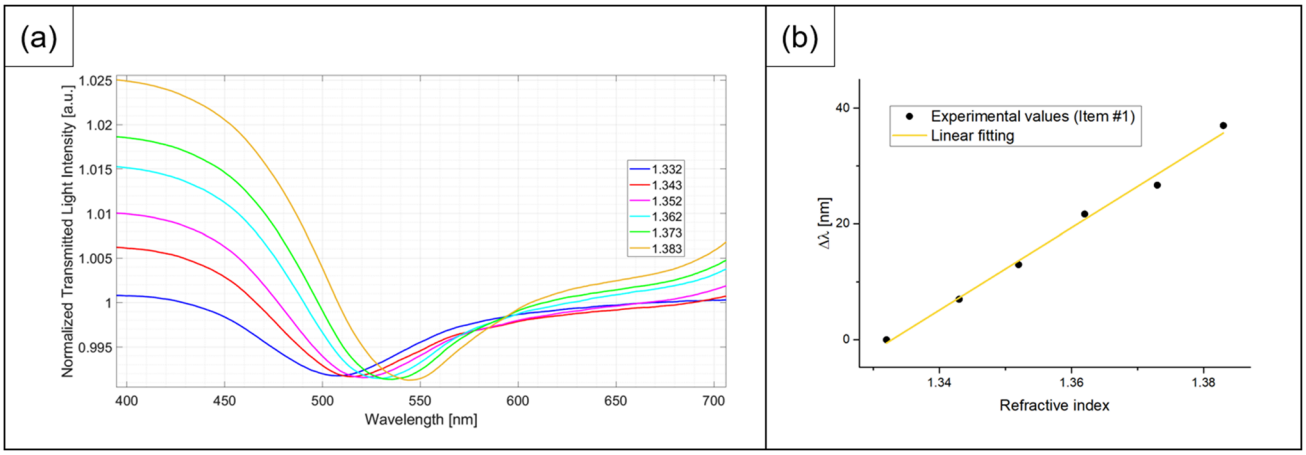

Fig. 14 Experimentally determined SPR spectra for the 3D printed item #1: (**a**) SPR spectra at different refractive index value. (**b**) Resonance wavelength variation ($\Delta\lambda$), calculated with respect to water ($n = 1.332$), along with the linear fitting of the experimental data

Table 4 Experimentally determined coefficients of Eq. (1): estimated values and standard errors

$\beta_0^{(1)}$		$\beta_1^{(1)}$		
Value	St. error	Value	St. error	Adj-R^2
−948.47	42.15	711.63	31.04	0.9906

(item #4) presented a sensitivity equal to 779 nm/RIU within the investigated refractive index interval (ranging between 1.33 and 1.38). Conversely, the SPR sensor characterized by a lower value of roughness (item #1) presented a sensitivity of 712 nm/RIU within the investigated refractive index interval (ranging between 1.33 and 1.38). The comparison between the linear responses of the SPR sensors items #1 and #4 (fitted lines reported in Figs. 14b and 15b) is also reported in Fig. 16.

In the case of SPR sensors based on multimodal optical waveguides, like the one presented in this work, the propagated light produces several angles/wavelengths that excite the SPR phenomena. Therefore, the SPR dips at different bulk solutions (1.33 − 1.38) are a convolution of several peaks, each for one specific propagated mode in the waveguide (thus, to a specific angle of incidence) [37]. More specifically, the angles associated with higher-order modes are the most sensitive to the SPR phenomena. Hence, by opportunely exciting a high number of modes by exploiting the scattering of the roughness, the SPR bulk sensitivity (in terms of bulk refractive index variation) results increased at the expense of a worsening of the signal-to-noise ratio [37]. So, when the surface roughness changes, the guided light is differently scattered by changing the number of modes in the guided light and the SPR phenomena. In particular, when the roughness increases, the scattering of the guided light increases, and the SPR sensitivity improves. This aspect in the bulk sensitivity (the enhancement due to the higher-order modes) is evident when the bulk presents high refractive

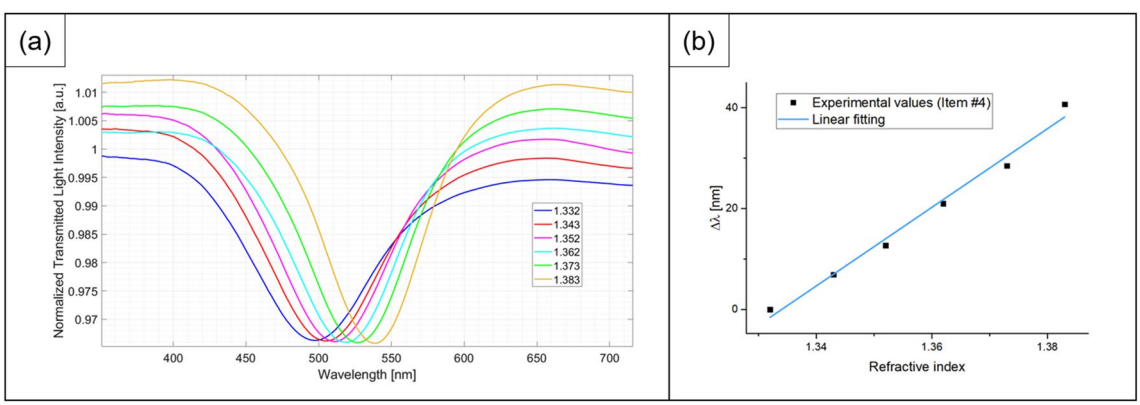

Fig. 15 Experimentally determined SPR spectra for the 3D printed item #4: (**a**) SPR spectra at different refractive index values. (**b**) Resonance wavelength variation ($\Delta\lambda$), calculated with respect to water ($n = 1.332$), along with the linear fitting of the experimental data

Table 5 Experimentally determined coefficients of Eq. (2): estimated values and standard errors

$\beta_0^{(4)}$		$\beta_1^{(4)}$		
Value	St. error	Value	St. error	Adj-R^2
−1039.82	61.49	779.46	45.29	0.9834

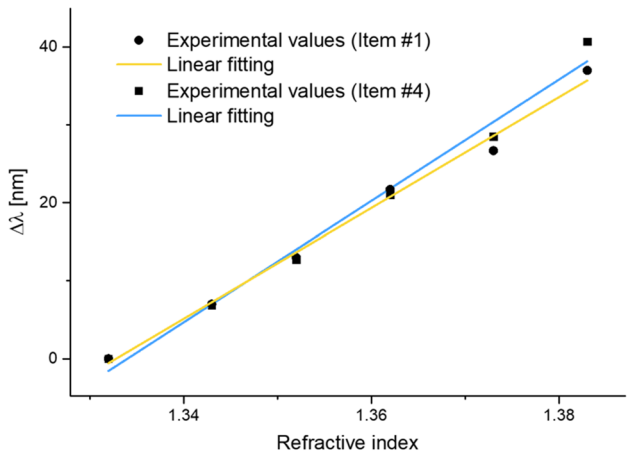

Fig. 16 Comparison between linear responses of items #1 and #4 in terms of the resonance wavelength variation ($\Delta\lambda$), calculated with respect to water ($n = 1.332$), versus refractive index value (linear fittings of the experimental data Fig. 14b and Fig. 15b)

indices (in an RI range between 1.35 and 1.38) [30], as shown also in Fig. 16.

The obtained results allowed to find a way to optimize the performance of the developed SPR sensor (i.e., its sensitivity) within a precise operative range of refractive index values to be measured by properly arranging the placement of the 3D printed parts on the building platform with the aim to modulate its surface roughness.

4 Conclusions

In this work, a polymer-based SPR sensor was designed and manufactured via an inkjet 3D printing technique, in line with a manufacturing approach already proposed by the authors [26]. Next, with the aim to understand how the surface roughness of the 3D printed sensor affects its performance, a surface finish quality assessment was performed through a profilometry test. A Phase I distribution-free quality monitoring investigation based on a recursive segmentation and permutation RS/P procedure revealed that the surface quality (i.e., the surface roughness expressed by measures R_a and R_z) for a pilot production run of sensors strictly depends on the placement of the 3D printed parts on the building platform. In fact, according to the RS/P analysis outcome, different changepoints, i.e., shifts in the location and in the dispersion (p-value < 0.05), have been found for both the investigated R_a and R_z parameters. The identified root cause to these results is related to the fact that the distribution of the peaks and valleys in the parts' surface is more uniform when only a one-direction movement of the printhead along X-axis is necessary to build them. Conversely, XY-axis movements during the fabrication process lead to a surface characterized by uneven droplet distribution with thin irregular spikes. Thus, two different clusters of items were identified based on their surface quality. In particular, R_a was equal to 0.93 ± 0.02 μm and R_z was equal to 9.05 ± 0.33 µm for the first identified cluster of items (sensors #1, #2, and #5). While, R_a was equal to about 1.21 ± 0.05 μm and R_z was equal to 19.77 ± 1.34 μm for the second cluster of items (sensors #3 and #4).

Next, the optical characterization of SPR sensors showing different surface roughness properties was carried out by using several liquids with different refractive index values (ranging between 1.332 to 1.383) as the surrounding medium for the gold nanofilm deposited upon the polymer waveguide. The aim was to relate the optical performances expressed as bulk sensitivity ($S_n = \Delta\lambda/\Delta n$) to the surface roughness of the 3D printed sensors. The obtained results unveiled that a higher bulk sensitivity (S_n), equal to 779 nm/RIU, is achieved when they are characterized by a higher surface roughness, i.e., for the second identified cluster of items, for the investigated interval of refractive index values. Conversely, a lower bulk sensitivity (S_n), equal to 712 nm/RIU, is obtained for lower values of surface roughness. So, a higher bulk sensitivity (S_n) for the developed SPR sensor is attained when higher values of surface roughness are achieved, in a similar way to the SPR sensors based on light-diffusing fibers [30]. Based on these findings, it is suggested to arrange the 3D printed parts' placement on the building platform with the aim of properly controlling the surface roughness by setting up sacrificial items in precise positions of the building platform. In this way, the needed performance to achieve precise operative condition will be guaranteed. Furthermore, the findings of this paper are encouraging to investigate the development of new strategies within the field of functional additive manufacturing to improve the surface roughness of SPR sensors by exploiting tailoring procedure on a micro- and nanoscale. In detail, the control on the micro-scale can be achieved through the 3D printing process itself, while at the nanoscale, it can be attained by using a proper functionalization processes by growing nanostructures suitable for the purpose.

Supplementary Information The online version contains supplementary material available at https://doi.org/10.1007/s00170-024-13649-x.

Author contribution Lorena Saitta wrote the paper, performed device design and manufacturing, and carried out the quality control analysis; Francesco Arcadio run the numerical and experimental tests and reviewed the paper; Giovanni Celano carried out the quality control analysis and reviewed the paper; Claudia Sergi run the surface roughness measurements; Gianluca Cicala, Nunzio Cennamo, Luigi Zeni, and Claudio Tosto reviewed the paper.

Funding Open access funding provided by Università degli Studi di Catania within the CRUI-CARE Agreement. The research was funded by the European Union (NextGeneration EU) through the MUR-PNRR project SAMOTHRACE (CUP: E63C2200090000).

Declarations

Competing interests The authors declare no competing interests.

Disclaimer The funders had no role in the design of the study; in the collection, analyses, or interpretation of data; in the writing of the manuscript; or in the decision to publish the results.

Open Access This article is licensed under a Creative Commons Attribution 4.0 International License, which permits use, sharing, adaptation, distribution and reproduction in any medium or format, as long as you give appropriate credit to the original author(s) and the source, provide a link to the Creative Commons licence, and indicate if changes were made. The images or other third party material in this article are included in the article's Creative Commons licence, unless indicated otherwise in a credit line to the material. If material is not included in the article's Creative Commons licence and your intended use is not permitted by statutory regulation or exceeds the permitted use, you will need to obtain permission directly from the copyright holder. To view a copy of this licence, visit http://creativecommons.org/licenses/by/4.0/.

References

1. Suvarnaphaet P, Pechprasarn S (2018) Enhancement of long-range surface plasmon excitation, dynamic range and figure of merit using a dielectric resonant cavity. Sensors (Switzerland) 18. https://doi.org/10.3390/s18092757
2. Shen M, Learkthanakhachon S, Pechprasarn S et al (2018) Adjustable microscopic measurement of nanogap waveguide and plasmonic structures. Appl Opt 57:3453. https://doi.org/10.1364/ao.57.003453
3. Hodnik V, Anderluh G (2009) Toxin detection by surface plasmon resonance. Sensors 9:1339–1354. https://doi.org/10.3390/s9031339
4. Shankaran DR, Gobi KV, Miura N (2007) Recent advancements in surface plasmon resonance immunosensors for detection of small molecules of biomedical, food and environmental interest. Sens Actuators B Chem 121:158–177. https://doi.org/10.1016/j.snb.2006.09.014
5. Yanase Y, Hiragun T, Ishii K et al (2014) Surface plasmon resonance for cell-based clinical diagnosis. Sensors (Switzerland) 14:4948–4959
6. Masson JF (2017) Surface plasmon resonance clinical biosensors for medical diagnostics. ACS Sens 2:16–30
7. Tang L, Li J (2017) Plasmon-based colorimetric nanosensors for ultrasensitive molecular diagnostics. ACS Sens 2:857–875
8. Wei H, Hossein Abtahi SM, Vikesland PJ (2015) Plasmonic colorimetric and SERS sensors for environmental analysis. Environ Sci Nano 2:120–135
9. Somekh MG, Pechprasarn S (2017) Surface plasmon, surface wave, and enhanced evanescent wave microscopy. Handbook of photonics for biomedical engineering. Springer, Netherlands, pp 503–543
10. Kik PG, Brongersma ML (2007) Surface plasmon nanophotonics. Dordrecht: Springer Netherlands, 1–9
11. Wang C, Ho HP, Shum P (2013) High performance spectral-phase surface plasmon resonance biosensors based on single- and double-layer schemes. Opt Commun 291:470–475. https://doi.org/10.1016/j.optcom.2012.10.064
12. Kurihara K, Suzuki K (1991) Theoretical understanding of an absorption-based surface plasmon resonance sensor based on Kretchmann's theory. Pockrand I Surf Sci 32:696–701. https://doi.org/10.1021/ac010820
13. Crowell J, Ritchie RH (1970) Surface-plasmon effect in the reflectance of a metal. J Opt Soc Am 60:794–799
14. Hoffmann A, Lenkefi Z, Szentirmay Z (1998) Effect of roughness on surface plasmon scattering in gold films. J Phys Condens Matter 10(24):5503
15. Chen X, Pan M, Jiang K (2010) Sensitivity enhancement of SPR biosensor by improving surface quality of glass slides. Microelectron Eng 87:790–792. https://doi.org/10.1016/j.mee.2009.11.092
16. Ritchie RH, Arakawa ET, Cowan JJ, Hamm RN (1968) Surface-plasmon resonance effect in grating diffraction. Phys Rev Lett 21:1530–1533
17. Braundmeier AJ, Arakawa ET (1974) Effect of surface roughness on surface plasmon resonance absorption. J Phw Chem Solids 35:5–17
18. Fontana E, Pantell RH (1988) Characterization of multilayer rough surfaces by use of surface-plasmon spectroscopy. Phys Rev B 37(7):3164
19. Kolomenskii A et al (2009) Propagation length of surface plasmons in a metal film with roughness. Appl Opt 48(30):5683–5691
20. Raether H (1988) Plasmons on smooth and rough surfaces and on gratings. Springer Tracts in Modern Physics 10
21. Kanso M, Cuenot S, Louarn G (2007) Roughness effect on the SPR measurements for an optical fibre configuration: experimental and numerical approaches. J Opt A: Pure Appl Opt 9:586–592. https://doi.org/10.1088/1464-4258/9/7/008
22. Treebupachatsakul T, Shinnakerdchoke S, Pechprasarn S (2021) Analysis of effects of surface roughness on sensing performance of surface plasmon resonance detection for refractive index sensing application. Sensors 21. https://doi.org/10.3390/s21186164
23. Schug C, Schempp S, Lamparter P, Steeb S (1999) Surface roughness of sputter-deposited gold films: a combined X-ray technique and AFM study. Surf Interface Anal 27:670–677. https://doi.org/10.1002/(SICI)1096-9918(199907)27:7%3c670::AID-SIA558%3e3.0.CO;2-1
24. Treebupachatsakul T, Shinnakerdchoke S, Pechprasarn S (2023) Sensing mechanisms of rough plasmonic surfaces for protein binding of surface plasmon resonance detection. Sensors 23. https://doi.org/10.3390/s23073377
25. Saitta L, Arcadio F, Celano G et al (2023) Design and manufacturing of a surface plasmon resonance sensor based on inkjet 3D printing for simultaneous measurements of refractive index and temperature. Int J Adv Manuf Technol 124:2261–2278. https://doi.org/10.1007/s00170-022-10614-4
26. Cennamo N, Saitta L, Tosto C et al (2021) Microstructured surface plasmon resonance sensor based on inkjet 3D printing using photocurable resins with tailored refractive index. Polymers (Basel) 13. https://doi.org/10.3390/polym13152518
27. Go J, Schiffres SN, Stevens AG, Hart AJ (2017) Rate limits of additive manufacturing by fused filament fabrication and guidelines for high-throughput system design. Addit Manuf 16:1–11. https://doi.org/10.1016/j.addma.2017.03.007
28. Chand R, Sharma VS, Trehan R et al (2023) Investigating the dimensional accuracy and surface roughness for 3D printed parts using a multi-jet printer. J Mater Eng Perform 32:1145–1159. https://doi.org/10.1007/s11665-022-07153-0
29. Araki S, Ryosuke T, Kazuhiko T (2018) High-speed additive manufacturing process using variable motion trajectory. In: IEEE Conference on Control Technology and Applications (CCTA). IEEE 483–488
30. Cennamo N, Zeni L, Catalano E, Arcadio F, Minardo A (2018) Refractive index sensing through surface plasmon resonance in

light-diffusing fibers. Appl Sci 8:1172. https://doi.org/10.3390/app8071172
31. Kumar K, Kumar GS (2015) An experimental and theoretical investigation of surface roughness of poly-jet printed parts. Virtual Phys Prototyp 10:23–34. https://doi.org/10.1080/17452759.2014.999218
32. Aslani KE et al (2019) Surface roughness optimization of poly-jet 3D printing using Grey Taguchi method. International Conference on Control, Artificial Intelligence, Robotics and Optimization (ICCAIRO). IEEE 213–218
33. Kamble P, Mittal Y, Gote G et al (2024) A mathematical surface roughness model for objects made by material jetting. Prog Addit Manuf. https://doi.org/10.1007/s40964-024-00573-5
34. Kechagias JD, Maropoulos S (2015) An investigation of sloped surface roughness of direct poly-jet 3D printing. In: Proceedings of the International Conference on Industrial Engineering - INDE (pp 150–153)
35. Cazón A, Morer P, Matey L (2014) PolyJet technology for product prototyping: tensile strength and surface roughness properties. Proc Inst Mech Eng B J Eng Manuf 228:1664–1675. https://doi.org/10.1177/0954405413518515
36. Vidakis N, Petousis M, Vaxevanidis N, Kechagias J (2020) Surface roughness investigation of poly-jet 3D printing. Mathematics 8:1–14. https://doi.org/10.3390/math8101758
37. Kanso M, Cuenot S, Louarn G (2008) Sensitivity of optical fiber sensor based on surface plasmon resonance: Modeling and experiments. Plasmonics 3:49–57. https://doi.org/10.1007/s11468-008-9055-1
38. Xiao J, Pan F, Xia H et al (2018) Computational study of single droplet deposition on randomly rough surfaces: surface morphological effect on droplet impact dynamics. Ind Eng Chem Res 57:7664–7675. https://doi.org/10.1021/acs.iecr.8b00418
39. Srivastava T, Jena SK, Kondaraju S (2021) Droplet impact and spreading on inclined surfaces. Langmuir 37:13737–13745. https://doi.org/10.1021/acs.langmuir.1c02457
40. Du J, Zhang Y, Min Q (2021) Numerical investigations of the spreading and retraction dynamics of viscous droplets impact on solid surfaces. Colloids Surf A Physicochem Eng Asp 609. https://doi.org/10.1016/j.colsurfa.2020.125649
41. Han X, Li J, Tang X, et al (2022) Droplet bouncing: fundamentals, regulations, and applications. Small 18
42. Capizzi G, Masarotto G (2013) Phase I distribution-free analysis of univariate data. J Qual Technol 45:273–284. https://doi.org/10.1080/00224065.2013.11917938

Publisher's Note Springer Nature remains neutral with regard to jurisdictional claims in published maps and institutional affiliations.